

Biocompatible Soft Fluidic Strain and Force Sensors for Wearable Devices

Siyi Xu, Daniel M. Vogt, Wen-Hao Hsu, John Osborne, Timothy Walsh, Jonathan R. Foster, Sarah K. Sullivan, Vincent C. Smith, Andreas W. Rousing, Eugene C. Goldfield, and Robert J. Wood*

Fluidic soft sensors have been widely used in wearable devices for human motion capturing. However, thus far, the biocompatibility of the conductive liquid, the linearity of the sensing signal, and the hysteresis between the loading and release processes have limited the sensing quality as well as the applications of these sensors. In this paper, silicone based strain and force sensors composed of a novel biocompatible conductive liquid (potassium iodide and glycerol solution) are introduced. The strain sensors exhibit negligible hysteresis up to 5 Hz, with a gauge factor of 2.2 at 1 Hz. The force sensors feature a novel multifunctional layered structure, with microcylinder-filled channels to achieve high linearity, low hysteresis (5.3% hysteresis at 1 Hz), and good sensitivity (100% resistance increase at a 5 N load). The sensors' gauge factors are stable at various temperatures and humidity levels. These biocompatible, low hysteresis, and high linearity sensors are promising for safe and reliable diagnostic devices, wearable motion capture, and compliant human–computer interfaces.

1. Introduction

Soft sensors, as a key component of soft electronic devices, have recently become prevalent in various research fields such as soft robotics,^[1–4] wearable robotics,^[5–10] and medical devices.^[11,12]

S. Xu, D. M. Vogt, Prof. R. J. Wood
John A. Paulson School of Engineering and Applied Sciences
Harvard University
Cambridge, MA 02138, USA
E-mail: rjwood@seas.harvard.edu

S. Xu, D. M. Vogt, Dr. W.-H. Hsu, J. Osborne, Dr. T. Walsh, J. R. Foster,
S. K. Sullivan, A. W. Rousing, Prof. E. C. Goldfield, Prof. R. J. Wood
Wyss Institute for Biologically Inspired Engineering
Harvard University
Boston, MA 02115, USA

Dr. V. C. Smith, Prof. E. C. Goldfield
Beth Israel Deaconess Medical Center
Boston, MA 02115, USA

Prof. E. C. Goldfield
Harvard Medical School
Harvard University
Boston, MA 02115, USA

Prof. E. C. Goldfield
Boston Children's Hospital
Boston, MA 02115, USA

 The ORCID identification number(s) for the author(s) of this article can be found under <https://doi.org/10.1002/adfm.201807058>.

DOI: 10.1002/adfm.201807058

These soft devices possess desirable properties such as high compliance, long life time, low weight, and low cost, making them more appealing compared to conventional rigid electronic sensors and actuators in many human-centric applications.

Soft material encapsulated conductive liquid sensors have been widely used in wearable robotics due to their high sensitivities, long life time, low cost, and simple fabrication processes. The most popular conductor is the liquid metal, Eutectic gallium–indium, or eGaIn.^[13–15] EGaIn-based sensors have been adopted in artificial skins,^[16,17] soft sensing gloves,^[18,19] and soft sensing suits^[20,21] for both strain and force measurements. Other types of conductive liquids, such as ionic liquids (ILs)^[22,23] and organic solutions,^[24] have also been studied to

develop wearable sensing devices. However, there are at least two challenges that limit these liquid conductors' use in soft sensors. First, it has, thus far, been challenging to obtain a linear response with fluidic sensors for force detection. Previous work^[25–27] has generally shown that, when a normal force is applied to a microchannel filled with a conductive liquid, the resistance change is exponential. This nonlinear performance not only limits the application of the conductive liquid sensors, but also reduces their dynamic range due to saturation of signal conditioning circuitry. Second, most conductive liquids adopted, thus far, for soft sensors (eGaIn, ionic liquids (IL), and organic solutions) are not sufficiently safe for applications on or within the human body. Although a biocompatible electrolyte–glycerol solution has been recently demonstrated for surgical tools,^[11] the conductivity of the solution is relatively low, and the material properties of such solutions have not been studied.

In this paper, we propose a novel biocompatible conductive liquid composed of potassium iodide and glycerol (KI-Gly). Compared to existing biocompatible solutions,^[11] this conductor improves the conductivity by a factor of four, and exhibits similar stability in air. With the KI-Gly solution, we develop high linearity and low hysteresis fluid-based KI-Gly strain and force sensors for safe and accurate human motion detection. Our strain sensors require low forces to achieve large deformations, and the sensor signal follows the same path during the loading and unloading processes. Our force sensors consist of a novel multilayer architecture with channels embedded with fillers.

We describe in detail how this architecture enables high resolution, high linearity, and low hysteresis. Additionally, we explore the sensor behavior over a temperature range of 15.0–65.0 °C and humidity range of 40.0–80.0% RH. We show that although the sensors' baseline resistances vary due to the external environment, their sensitivities stay relatively stable. Finally, we demonstrate the utilization of the fluidic sensors for precise human motion tracking by attaching both strain and force sensors to a human hand. By comparing sensor measurements with motion capture, we show that our sensors can successfully track motion and measure interaction forces.

2. Results and Discussion

2.1. Properties of the Biocompatible Conductive Electrolyte–Glycerol Solution

The conductive solution was prepared by dissolving a biocompatible electrolyte, potassium iodide (KI), into glycerol with a centrifugal mixer (ARE-310, THINKY, USA) for 20 min. Glycerol, a low toxicity viscous liquid commonly used in pharmaceuticals and cosmetics, shares some physical properties with water, such as the solubility of halide compounds.^[28] Glycerol breaks the crystal structure of KI during dissolution and forms freely moving potassium cations (K^+) and iodide ions (I^-), enabling the conductivity of the liquid (Figure 1a). However, glycerol has a much lower evaporation rate than

water due to higher intermolecular forces, resulting in greater stability of the KI-Gly solution. Related, the longer chain glycerol molecules make them less likely to penetrate through the silicone substrate of the soft sensors. These properties make glycerol solutions more stable and durable when embedded in silicone materials compared to aqueous electrolyte solutions, and thus tend to improve the lifetime of these soft sensors.

In previous work, soft sensors have been fabricated using sodium chloride–glycerol (NaCl-Gly) solutions. However, these solutions have low conductivities, and require long preparation times (10 h) due to the limited solubility of NaCl in glycerol. Their low conductivities not only increase the difficulty of designing the signal conditioning circuitry, but also decrease the signal-to-noise ratio (SNR) during sensor operation. To address these issues, we increased the conductivity of the solution by replacing NaCl with a more soluble electrolyte, KI. KI reduces the new liquid (KI-Gly) resistivity by a factor of almost four (from 28.4 to 7.4 Ω m) compared to the old liquid (NaCl-Gly) and shortens the preparation time from 10 h to 20 min.

In addition to the improved conductivity, the KI-Gly solution has a lower viscosity compared to the NaCl-Gly solution. According to the empirical equations derived by Jones and Dole,^[29,30] ions dissolved in a solvent may potentially change the viscosity of the original solvent. This effect is driven by the ion–ion interactions and ion–solvent interactions, represented by solubility A and B coefficients in Equation (1), respectively. The Jones and Dole relationship between viscosity of the solvent before and after dissolving electrolytes is shown in Equation (1)^[29]

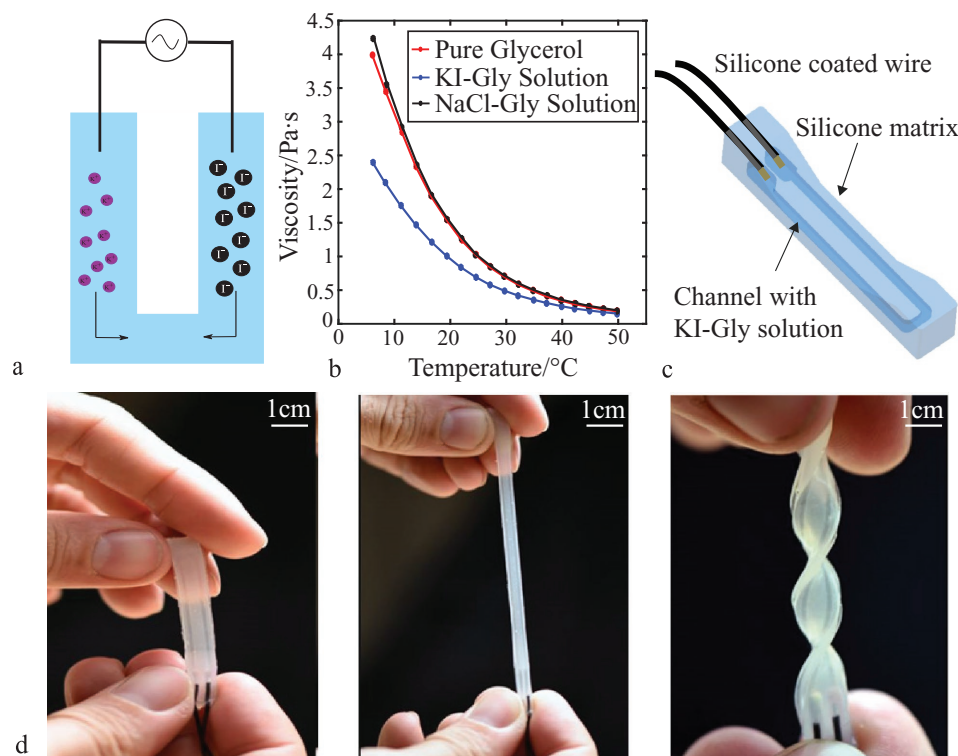


Figure 1. a) Schematic of the conduction mechanism of the KI-Gly solution in the sensor channel. b) Viscosity variation of glycerol, KI-Gly solution, and NaCl-Gly solution at temperatures ranging from 5.0 to 50.0 °C. c) Schematic of the strain sensor. d–f) Demonstration of the stretchability and flexibility of a soft strain sensor with the strain sensor at d) the original length, e) stretched, and f) twisted.

$$\frac{\eta}{\eta_1} = 1 + A\sqrt{c} + Bc \quad (1)$$

where η is the viscosity of the solution, η_1 is the viscosity of the solvent, A and B are solubility coefficients, and c is the concentration of the solution.

For solutions with concentrations between 1 M and 10 M, the \sqrt{c} term in the Jones and Dole equation is small and the ion–ion interaction is negligible. Therefore, the viscosity of the solution is mainly determined by the coefficient B , which describes ion–solution interactions. The coefficient B for NaCl in glycerol is 0.463,^[30] while that of KI is -0.178 .^[30] This illustrates that dissolving NaCl in glycerol has the potential to increase the solution viscosity, while adding KI tends to reduce it. Figure 1b shows the experimental viscosity of the NaCl-Gly solution, pure glycerol, and the KI-Gly solution at temperatures ranging from 5.0 to 50.0 °C, measured with a Rheometer (AR-G2, TA Instruments Ltd, USA) at constant shear rate (3 rad s⁻¹). The viscosity of these three solutions decreases exponentially as temperature increases, and the KI-Gly solution has a lower and more stable viscosity than either the pure glycerol or the NaCl-Gly solution. Stable viscosity leads to high thermal stability and low hysteresis during loading and unloading, which will be discussed in later sections.

2.2. Strain Sensors

2.2.1. Strain Sensor Design

The strain sensor consists of three components: a silicone substrate, a conductive liquid-filled channel, and silicone-coated wires. To minimize the mechanical impedance of the soft sensors, we chose the silicone rubber EcoFlex 0030 (Smooth-on, PA, USA), which has a low Young's modulus (70 kPa) and high failure strain (900%),^[31] as the sensor matrix. EcoFlex 0030 has successfully served as a biocompatible and stretchable substrate in a variety of wearable sensors and actuators. The elastomer base is designed with a thickness gradient, with sensor height decreasing from the two ends to the center. This geometry helps focus the strain on the portion of the sensor that contains the microchannel and away from the connecting wires. A U-shaped channel (1.0 mm high \times 0.5 mm wide) is embedded in the silicone substrate. The U-shaped design helps to locate the electrical wire at the same side of the sensor. The channel's specific dimensions ensure the sensor resistance is approximately 300 k Ω before stretching, enabling a low noise signal from the signal conditioning electronics. The silicone coated wires are used to improve the soft-to-rigid connection from soft sensors to electronics and also for chemical compatibility with the substrate to facilitate bonding. Figure 1c shows the schematic of a strain sensor. Figure 1d–f shows the soft sensor under high strain, demonstrating its high flexibility and stretchability.

2.2.2. Strain Sensor Properties

To investigate the resistance changes of the strain sensor under unidirectional stretch, we used a dynamic mechanical analyzer

(ElectroForce 3200, Bose, DE, DMA) to apply stretch forces to the sensors. The electrical circuit for measuring the sensor response is depicted in the Supporting Information (Figure S1). We stretched the sensor up to 50% strain, and recorded the analog voltage signal as well as the simultaneous force and displacement at four stretching speeds: 0.25, 0.5, 1, and 2 Hz (the fastest full-range finger movement is 2 Hz).^[32] Due to the limitations of the DMA, the sensor was only able to be stretched to 25% at 2 Hz. From Figure 2a, the sensor has a gauge factor of 2.2 under 50% strain and remains constant across various tested speeds. In addition, we observed low hysteresis and an SNR greater than 50 during loading and release processes.

The behavior of the resistance change shows that, within the measurement range of 50% elongation and 1 Hz (25% for 2 Hz) stretching speed, the conductive liquid is able to follow the deformation of the channel and the substrate material behaves elastically. However, at higher loading speeds, the viscoelastic behavior of the liquid and elastomer may cause a delay in the sensor response. We studied the sensor's performance with the DMA by applying a unidirectional sinusoidal motion to the sensor with 5.0 mm (20% strain) dynamic amplitude. The frequency was varied from 1 to 10 Hz. As plotted in Figure 2b, at 1 Hz, the sensor is able to follow the stretching motion, with a relative resistance change of 30%. At low frequencies, the phase shift between the sinusoidal actuation and the sensor signal is negligible. At 5 Hz with a response time of 0.1 s, the sensor delay begins to appear, and the relative resistance change decreases to 15%. At 10 Hz, the sensor delays becomes more apparent while the voltage output amplitude continues to decrease (partially due to the DMA limit of 5.0 mm amplitude at 10 Hz). The observed delay in the sensor response is caused by the viscous flow of the liquid and the viscoelasticity of the elastomer. However, the viscous property of the substrate material below 10 Hz is negligible (see Table S1, Supporting Information). Therefore, a major limitation to the high frequency operation of the KI-Gly strain sensor is due to the viscosity of the liquid. However, for the application to human motion tracking, a bandwidth limit on the order of 5 Hz is sufficient.

To evaluate the reversibility and durability of the strain sensor, we conducted cyclic stretching and bending tests. The stretching test was performed by applying 50% strain at 0.25 Hz for 1000 repetitions using a material tester (Instron 5544A, Surplus Solutions LLC, RI, USA). Figure 2c compares the initial and last ten cycles, demonstrating consistent sensor performance. The variation in relative resistance change is within 5%, and no obvious delay exists. The cyclic bending test was conducted by indenting a 3.0 cm diameter cylinder perpendicularly to the sensor at 1 Hz with 1000 repetitions using the Instron. By comparing the first and last ten cycles (Figure 2d), we observed relatively constant bending responses over the 1000 cycles, with a maximum signal variation less than 6%.

To quantify the effect of bending on the sensor, we measured the resistance change at different curvature and strain values. We used eight cylinders with different diameters (4.0, 6.0, 10.0, 22.0, 34.0, 38.0, 63.5, and 76.0 mm) and stretched the sensors to 0%, 50%, and 100% strain. The sensor resistance at each strain was measured three times. The average values and standard deviations are plotted in Figure 2e. The resistance at bending

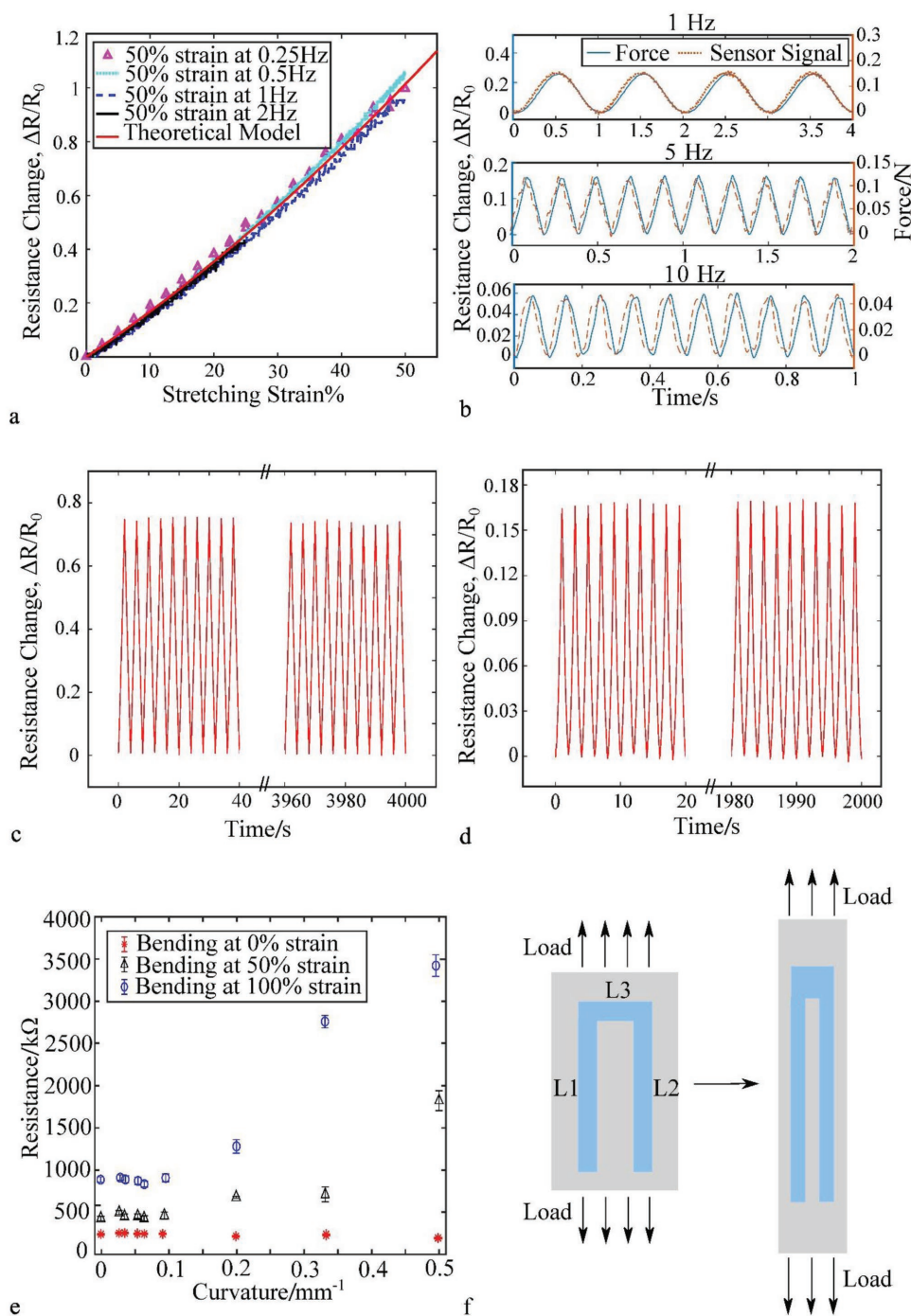


Figure 2. Characterization of conductive liquid soft strain sensors. a) Experimental results of resistance change ($\Delta R/R_0$) as a function of the applied strain at different stretching speeds. b) Measurement of sensor response and simultaneous force under mechanical load with frequencies of 1, 5, and 10 Hz. c) Experimental resistance change ($\Delta R/R_0$) of initial and final ten cycles from a 1000 cycle stretching test. d) Experimental resistance change ($\Delta R/R_0$) of initial and final ten cycles from a 1000 cycle bending test. e) Investigation of resistance change of strain sensors at various curvatures and 0%, 50%, and 100% strain. Each data point is the average value of three measurements and the error bars represent corresponding standard deviations. f) Schematic of the strain sensor before and after stretching.

curvatures below 0.1 mm^{-1} does not change significantly for all strain values (within 5% of the resistance change), but increases dramatically at 50% and 100% strains for curvatures above 0.2 mm^{-1} . This is because the microchannel lengths

and cross-sectional areas do not differ much at low curvatures and low strains. However, at curvatures above 0.2 mm^{-1} and high strains (i.e., larger than 50%), the curved surface applies normal pressure to the microchannels. This causes a decrease

of the sensor cross-sectional area, and consequently leads to an increase in resistance.

The resistance change of the sensor under stretch is mainly due to the increase in length and decrease in cross-sectional area of the embedded channel. This behavior can be described with a Neo-Hookean hyperelastic material model. Figure 2f shows the channel geometry before and after stretch. During this process, the length of the longitudinal channels increases while the cross-sectional area decreases, and the length of the horizontal channel decreases while the cross-sectional area increases. A contact resistance exists between the electrode and the conductive liquid, and therefore a constant is multiplied to the equation. The dashed line in Figure 2a indicates that the theoretical value (represented by Equation (1)) of the resistance change agrees with the experimental value below 50% strain. A detailed theoretical model is discussed in supplement information, but the change in resistance ($\Delta R/R_0$) is given by

$$\frac{\Delta R}{R_0} = c \cdot \frac{2L_1((1+\varepsilon)^2 - 1) + L_2\left(\frac{1}{1+\varepsilon} - 1\right)}{2L_1 + L_2} \quad (2)$$

where L_1 is the length of the longitudinal channel, L_2 is the length of the horizontal channel as shown in Figure 2f, c is the contact resistance constant, and ε is the strain.

2.3. Force Sensors

2.3.1. Force Sensor Design

The force sensor contains two functional layers: a sensing layer and a force amplification layer. The sensing layer consists of a silicone matrix made of a 3:1 mixture of Sylgard 184 (10:1) (Sylgard 184, Dow Corning, MI, USA) and Ecoflex 0030. A 0.5 mm square meander channel is embedded in the silicone mixture substrate. The channel is filled with 1 mm long, 0.5 mm diameter cylindrical fillers, and is injected with KI-Gly solution. The fillers are made from poly-methyl methacrylate (PMMA) optical fibers, which have a much higher modulus than the silicone substrate and are not electrically conductive. The channel cross section of the 3D printed mold is designed to be a square with a 0.5 mm side length. However, after casting with silicone, the cross section becomes a semicircle with a height of 0.5 mm and width of 0.8 mm. Figure 3a shows the schematic of the force sensor and its cross section. Figure 3b,c shows the channel with cylindrical fillers and its cross section under confocal microscopy, respectively. A force amplifying layer containing an 8.0 mm² rigid indenter is added to the sensing layer to reduce the contact area between objects and the sensor. When applying forces, the indenter pinches the soft channel perpendicularly to

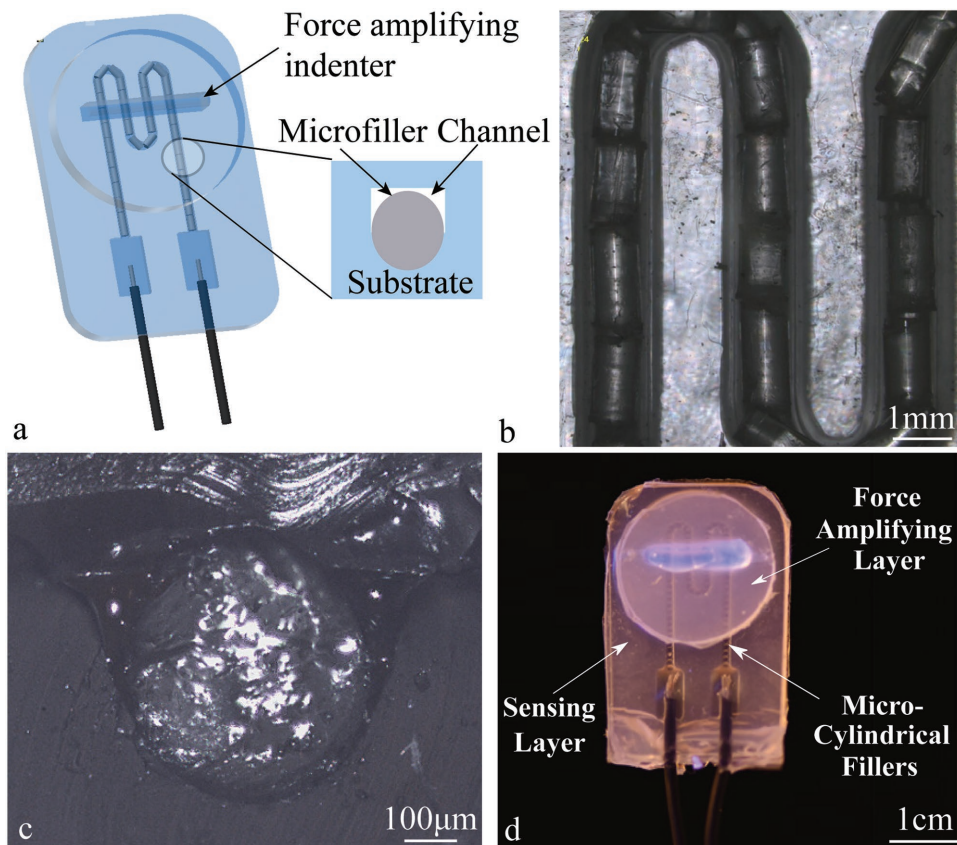


Figure 3. a) Schematic of force sensor and cross section of channel with cylindrical fillers. b) Top view of microcylinder-filled channel under confocal microscopy. c) Cross section of microcylinder-filled channel under confocal microscopy. d) View of the force sensor under UV light with sensing layer and force amplifying layer labeled.

increase the generated pressure. The force amplifying layer substrate is made of Ecoflex 0010 silicone and is bonded to the sensing layer, leaving an empty slot between two layers. A liquid UV-curable adhesive is injected into the slot. The adhesive becomes a rigid acrylic after exposing under UV light, which functions as the indenter applying forces to the sensing layer. For wearable devices that require multidirectional sensing over a large area, a microscale rigid indenter array can be incorporated to retain sensor flexibility. Figure 3d shows the force sensor under UV light.

2.3.2. Linearity Improvements

The linearity of the sensor response under an applied force is mainly influenced by the channel deformation. In previous work on fluidic soft force sensors with rectangular channels, nonlinear response is observed.^[25–27] This behavior is caused primarily by the nonlinear relationship between the collapsed channel height and the applied normal force.^[27] This nonlinear response causes the sensitivity at low forces (i.e., less than 50% of the sensing range) to be 90% lower than that at high forces and reduces the SNR by a factor of 10 (assuming that the noise in the signal is not affected by loading). Therefore, the nonlinearity limits the dynamic range as well as the sensor resolution at low forces.

Previous studies have indicated that varying the channel width-to-height ratio or changing the channel cross-section geometry from rectangular to triangular improves the sensor linearity.^[26,33] However, these methods require complicated fabrication techniques (e.g., 3D micromachining processes), result in nonlinear response, and are difficult to tune the sensing regime smoothly. Another method of adding microspheres to the channel has been introduced to limit the sensor exponential behavior.^[34] These rigid microfillers prevent the collapse of the channel under high forces and at the same time enlarge the relative channel geometrical changes at low forces. This helps to alleviate the exponential resistance increase at high forces and increases the sensitivity at low forces. However, the microspheres are geometrically nonuniform along the channel direction, which leads to a nonuniform modification of the channel deformation. Furthermore, the spherical fillers move easily in the channel in a liquid environment under high pressures. Therefore, the enhanced sensor responses are not sufficiently durable and reliable.

To address these issues, we replaced the microspheres with microcylinders. Microcylinders uniformly support the channel under normal forces which avoids nonlinear channel deformations throughout the entire channel. Furthermore, microcylinders are less likely to move in the channel, which helps to improve the sensor durability and repeatability. We tested the force sensor with empty channels and both fillers using the Instron by applying a normal, uniformly distributed force to the force amplifying layer, and recorded the synchronized output signal using the signal conditioning circuit discussed above. **Figure 4a** compares sensors with empty channels at various elastomer moduli versus channels with spherical and cylindrical fillers. The

result demonstrates that by varying the elastomer moduli we can tune empty channel sensor range, but this does not significantly improve linearity. For all tested moduli, sensitivities at low forces (i.e., less than 50% of the sensing range) are only 10% of those at high forces. Furthermore, noticeable hysteresis exists during the loading and release processes. However, the sensor responses with both spherical and cylindrical fillers are much improved, relative to the nonlinearity and hysteresis of the empty channel. To characterize the linearity of the response with spherical and cylindrical fillers, we fit the curves with second order polynomials. The sensor with microcylinders has a higher linearity response with a lower second order prefactor of 0.026 N^{-2} , while that of microsphere-filled sensor is 0.046 N^{-2} . The microcylinder-filled sensor reaches a resistance change of 100% at 5.5 N of normal force.

In addition to incorporating microcylinders, we also replaced the commonly used substrate material Ecoflex 0030 with a 3:1 mixture of Ecoflex 0030 and 10:1 Sylgard 184 to increase the signal linearity. The addition of Sylgard 184 to Ecoflex 0030 greatly increase the stiffness of the substrate material. From the theoretical model developed in previous work,^[27] a higher stiffness substrate tends to increase the linearity of the sensor. One concern with linearizing the sensor response is that the sensor's sensitivity is sacrificed to obtain linearity. Therefore, we added a force-amplifying layer containing a rigid indenter to compensate for the sensitivity loss. Another advantage of this silicone mixture is that it has properties of both Sylgard 184 and Ecoflex 0030. Thus, it is able to plasma-bond to itself during the channel enclosure process and wet bond to Ecoflex 0010 when fabricating the force amplifying layer.

To test the robustness and repeatability of the sensor, we applied normal forces with the Instron for 1000 cycles. By comparing the initial and last ten cycles (**Figure 4b**), we found that the sensor shows less than 10% variation in the sensitivity after the tests, relative to the first ten cycles. A dynamic test was also conducted to characterize the sensor response time. We applied a 0.4 mm displacement to the sensor with frequencies ramping from 1 to 50 Hz. As plotted in **Figure 4c**, the sensor is able to follow the applied load at 1 Hz. As the frequency increases, we observed an amplitude loss and a phase shift between the applied load and the sensor response. Similar to the behavior of the strain sensor, these are mainly due to the viscoelasticity of the conductive liquid. To characterize the amplitude change, we plotted the amplitude frequency response from the DMA test in **Figure 4d**. The sensor response decreases by 6 dB at 50 Hz, but could still be clearly detected.

To study the force sensor under curved shapes, we bent a force sensor to five different curvatures (0, 0.08, 0.20, 0.30 mm^{-1}) and recorded its resistance under normal forces ranging from 0 to 5 N. From **Figure 4e**, the sensor resistance is relatively stable when unloaded at all tested curvatures (less than 5% variation), but increases significantly under normal forces at high curvatures (the sensor resistance doubles when the normal force exceeds 3 N and the curvature is larger than 0.1 mm^{-1}). This is because the microcylinders move out of the channel surface at high curvatures and are likely to block the channel (thereby reducing the

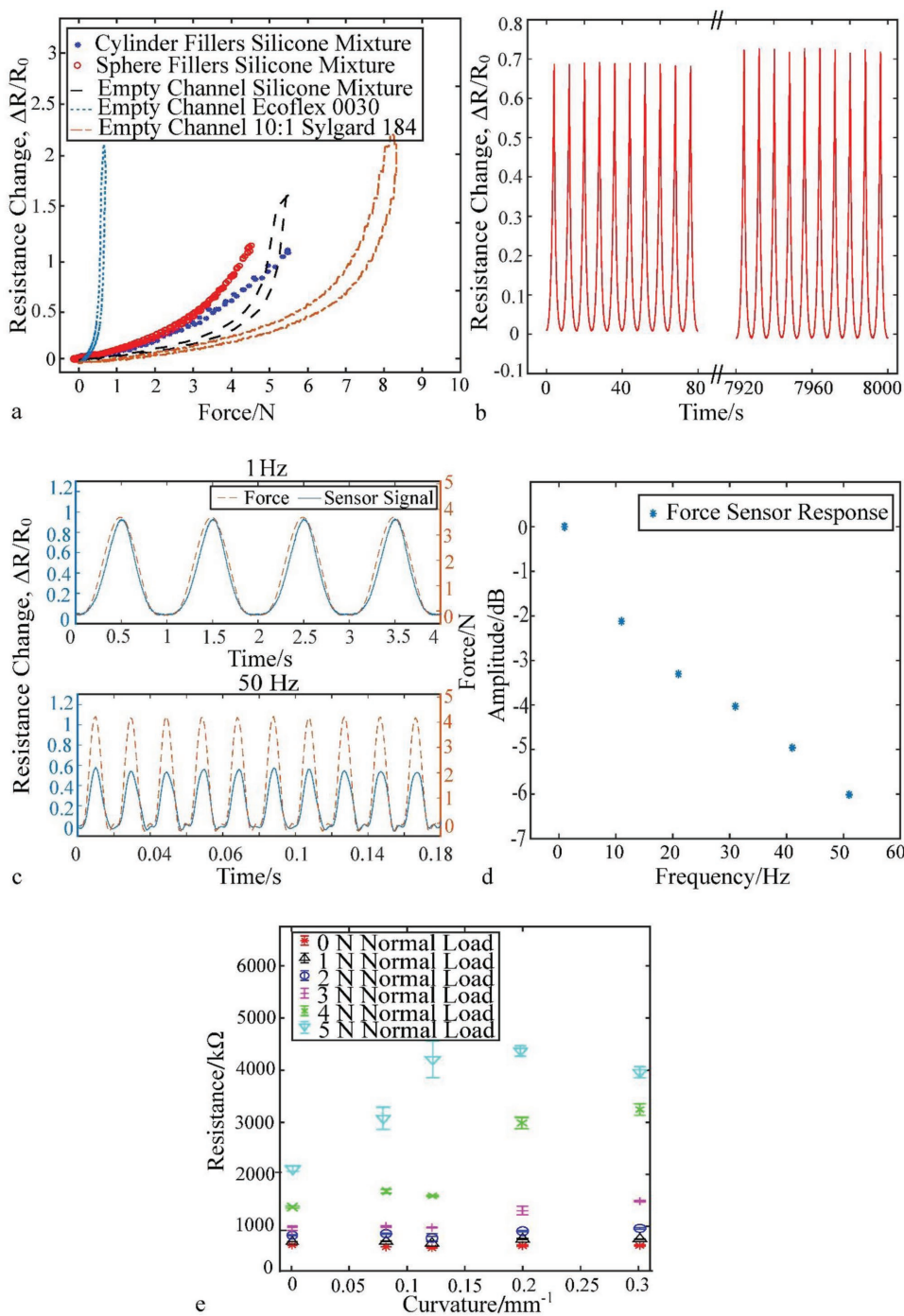


Figure 4. Characterization of the KI-Gly liquid force sensor. a) Force sensor relative resistance change ($\Delta R/R_0$) as a function of normal force with an empty channel at various elastomer moduli, microcylinder fillers, and microspheres fillers. b) Force sensor experimental resistance change ($\Delta R/R_0$) of the initial and final ten cycles from a 1000 cycle test. c) Measurements of force sensor response and simultaneous force under mechanical load at frequencies of 1 and 50 Hz. d) Force sensor signal amplitude as a function of loading frequency. e) Investigation of resistance change of force sensors at various curvatures under 0–5 N forces. Each data point is the average value of three measurements and the error bars represent the standard deviations.

cross-sectional area) under normal forces. However, for the application of wearable devices, force sensors are unlikely to experience large curvatures, and a tolerance of 0.1 mm^{-1} (bending radius lower than 10 mm) is sufficient.

2.3.3. Mechanical Model

The relative resistance change of the force sensor is achieved by the deformation of the channel. Figure 3a shows the channel

cross section. A similar deformation has been studied in previous work and is represented by Equation (3)^[34]

$$\frac{\Delta R}{R} = \frac{4L_1}{L_2} \left(\frac{r^2 - \frac{1}{4}\pi r^2}{(r-a)(r-\delta) + \frac{1}{2}a(r-\delta) - \frac{1}{2}\theta r^2} - 1 \right) \quad (3)$$

where r is the microfiller radius, a is the width of fiber in contact with the elastomer after compression, δ is the compression of the microfiber into the elastomer, L_1 is the width of the indenter, and L_2 is the overall channel length. A detailed theoretical model is discussed in Section 4 of the Supporting Information.

To estimate the force applied to the sensor, the force sensor can be seen as an isostress composite material in the vertical direction and an isostrain composite material in the horizontal direction. We used a Neo-Hookean model to describe the stress-compression relationship. The net force applied can be determined by a summation of the force of the elastomer region and the microchannel region

$$F = \sum_{i=1}^4 \mu_{\text{composite}_i} \left(\lambda^2 - \frac{1}{\lambda} \right) S_{\text{composite}_i} + \sum_{i=1}^5 \mu_{\text{elastomer}_i} \left(\lambda^2 - \frac{1}{\lambda} \right) S_{\text{elastomer}_i} \quad (4)$$

where F is the applied load, λ is the sensor compression, $\mu_{\text{composite}_i}$ is the shear modulus of the composite material, $\mu_{\text{elastomer}_i}$ is the shear modulus of the elastomer substrate, $S_{\text{elastomer}_i}$ is the indented elastomer area, and $S_{\text{composite}_i}$ is the indented composite area. (See Section 4 in the Supporting Information for a detailed discussion.)

The model discussed above reveals that the sensitivity and linearity of the sensor can be tuned by manipulating three factors: the thickness of the substrate, the radius of the microfiller, and the stiffness of the substrate material. Figure 5a–c shows the experimental measurements of sensor responses by varying each of the parameters above, respectively. We also plotted their corresponding theoretical predictions as a comparison. Moreover, we fit the curves with second order polynomials to study their linearity. This analysis shows that lower substrate thickness leads to higher sensitivity, but lower linearity. As is plotted in Figure 5a, the sensor reaches a 55% resistance increase at 3.5 N load with a 0.3 mm substrate thickness, while only a 32% resistance increase is achieved with a 1.2 mm substrate thickness at the same load. This is due to the thicker substrate requiring higher forces to achieve the same compression on the sensor channel, which directly influences channel deformation, and thus the variation in resistance. The fitted second order polynomials of the three curves show

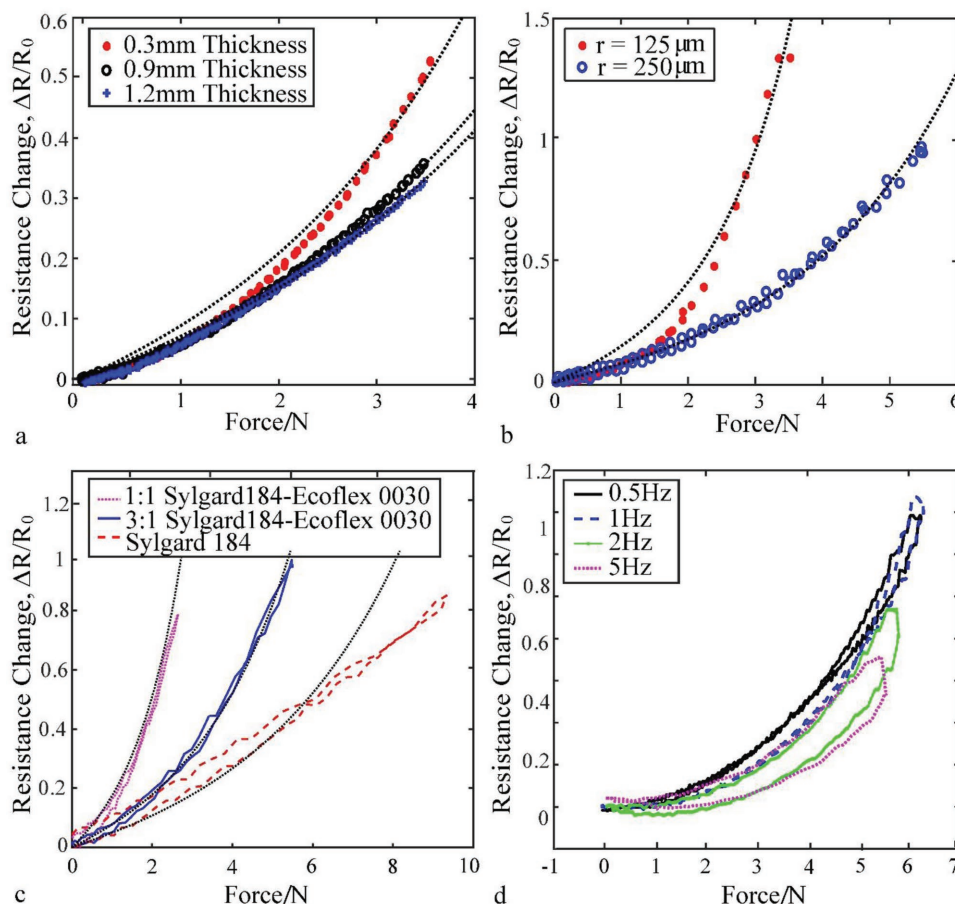


Figure 5. a) Experimental investigations on sensor sensitivity by varying substrate thickness from 0.3 to 1.2 mm and corresponding theoretical predictions. b) Experimental results on the influence of microfiller diameter on sensor sensitivity by testing 0.5 and 0.25 mm diameter microcylinders and corresponding theoretical predictions. c) Experimental investigations on varying substrate material stiffness and corresponding theoretical predictions. d) Experimental results of resistance change ($\Delta R/R_0$) as a function of applied force with 0.5, 1, 2, and 5 Hz loading speeds.

that, the polynomial for 0.3 mm substrate has the highest second order prefactor of 0.359 N^{-2} and thus the lowest linearity, while the ones with 0.9 and 1.2 mm substrates have lower prefactors of 0.017 and 0.011 N^{-2} , respectively. Second, reducing the microfiller radius increases sensitivity, but decrease linearity. As plotted in Figure 5b, the resistance increase of the sensor with 0.125 mm fillers is 130% at 3.5 N, while that of the sensor with 0.25 mm fillers is only less than 50%. However, the 0.125 mm fillers curve (with a second order prefactor of 0.151 N^{-2}) is less linear compared to the 0.25 mm curve (with a prefactor of 0.017 N^{-2}). This is due to the small rigid filler volume fraction of the sensor with 0.125 mm microcylinders. A lower volume fraction of rigid fillers causes a lower modulus of the sensor as the composite, which requires lower forces to generate channel deformations. For similar reasons, sensors with lower stiffness substrates tend to have higher sensitivity, but with greater nonlinearity. The sensor made of Sylgard 184 (10:1) substrate requires 8 N to reach a resistance increase of 70%, while the sensor with a 1:1 Sylgard 184-Ecoflex substrate only needs 2 N to achieve the same level, as is shown in Figure 5c. However, the 1:1 mixture curve has a lowest linearity with a second order prefactor of 0.102, while those of 3:1 mixture and Sylgard 184 (10:1) are 0.026 N^{-2} and 0.003 N^{-2} , respectively. Sensors with thicker substrates, smaller microfiller radius, and lower substrate stiffness have higher sensitivity, but also a more nonlinear signal response. Therefore, it is important to tailor each of these parameters to customize the sensor for various sensing ranges.

2.3.4. Hysteresis Analysis

Fluidic soft force sensors generally display large hysteresis as shown in previous studies on eGaIn soft sensors.^[25,27,34] The viscoelastic property of the soft substrate and the viscous flow of the liquid cause a delay of the conductive liquid when flowing back to the its original position after the load is removed, generating the hysteresis loop in the sensor responses. The magnitude of the hysteresis is mainly determined by the following factors: the viscosity of conductive liquid, the stiffness of the sensor substrate, the volume of the liquid being “squeezed” during loading and release, and the speed of the applied force. In our sensor, we reduced the sensor hysteresis in three ways. First, we used a relatively low viscosity KI-Gly solution compared to previously used glycerol solutions to generate faster liquid flow. Second, we reduced the amount of the liquid that flowed in and out of the channel. We achieved this by decreasing the cross-sectional area of the channel via the microcylinder fillers, as well as reducing the contact area between the sensing layer and the object. Third, we kept the stiffness of the silicone mixture relatively high. A high stiffness substrate is generally harder to deform and to squeeze the liquid during loading process, but has higher recovery energy to restore itself to its original state.

The effect of microfillers on reducing the hysteresis is illustrated in Figure 4a. Despite the increase in linearity of the signal (as discussed above), the sensor without microfillers has a much larger hysteresis loop compared to the sensors with microfillers. We tested the force sensor at various loading speeds: 0.5, 1, 2, and 5 Hz (Figure 5d). At low frequencies, the

hysteresis loop is negligible, with 8.6% and 5.3% (hysteresis loop area normalized to the area below signal curve) at 0.5 and 1 Hz, respectively. However, as the loading frequency increases, the hysteresis area increases to 76.9% and 109.1% at 2 and 5 Hz, respectively. In addition, the hysteresis loop is more pronounced at high loading forces. This is because the conductive liquid is not able to follow the force due to its viscosity at high loading speeds. Large forces require a high volume of liquid flow, which tends to result in a longer delay.

2.4. Sensor Properties

2.4.1. Temperature

One potential concern in using the KI-Gly solution as a sensor component is that the conductivity of the liquid varies as temperature fluctuates. This conductivity change is attributed to the exponential viscosity change of the liquid as a function of temperature as was already discussed. The conductivity of the liquid is determined by the freely moving dissolved ions. A liquid with low speed free ions is expected to have low conductivity compared to a liquid that contains fast drifting ions, and the drifting speed is inversely proportional to the viscosity of the liquid. In other words, high viscosity slows down the ion speed, and thus decreases conductivity. Although the KI-Gly solution we use has a relatively stable viscosity compared to previously used NaCl-Gly solutions, its conductivity still varies greatly.

We investigated the influence of temperature on the sensor resistance (same with liquid conductivity) with a controlled temperature and humidity chamber (LH10, Associated Environmental System, MA, USA). Both sensors were placed in the chamber at rest, and we varied the chamber temperature from 15.0 to 65.0 °C with an interval of 10.0 °C every 40 min. Sensor resistances were measured and recorded every 60 s with an LCR meter (880, BK Precision Corp., CA, USA). Figure 6a shows that as the temperature was raised from 15.0 to 65.0 °C, the strain sensor resistance decreased exponentially from 240 to 50 kΩ. In the first 10.0 °C increment, the resistance dropped greatly by 80.0 kΩ, but during the last 10.0 °C increment, the resistance dropped only 20.0 kΩ. The relationship between the sensor resistance and the environment temperature is expressed as Equation (5)

$$R = C \cdot \exp\left(\frac{Q}{KT}\right) \cdot \frac{L}{A} \quad (5)$$

where C is a fitting constant, Q is the activation energy, K is the Boltzmann constant, L is the length of the sensor channel, and A is the cross-sectional area of the sensor channel. To determine the relationship between resistance and temperature, we took the logarithm of Equation (5). We used the average resistance at each temperature and applied linear fit to the plot as shown in Figure 6b. The slope of the fitted line represents $\frac{Q}{K}$, which is 4286 K, and the fitting constant C is $1.6 \mu\Omega\text{m}$.

Importantly, the conductivity changes of the liquid due to temperature fluctuation do not have an influence on the sensitivity of the sensor when being stretched or compressed. This is because the relative resistance change (i.e., $\Delta R/R_0$) is not influenced by the resistivity of the liquid. We tested both strain and force sensors with the Instron at 10.0 °C, room temperature,

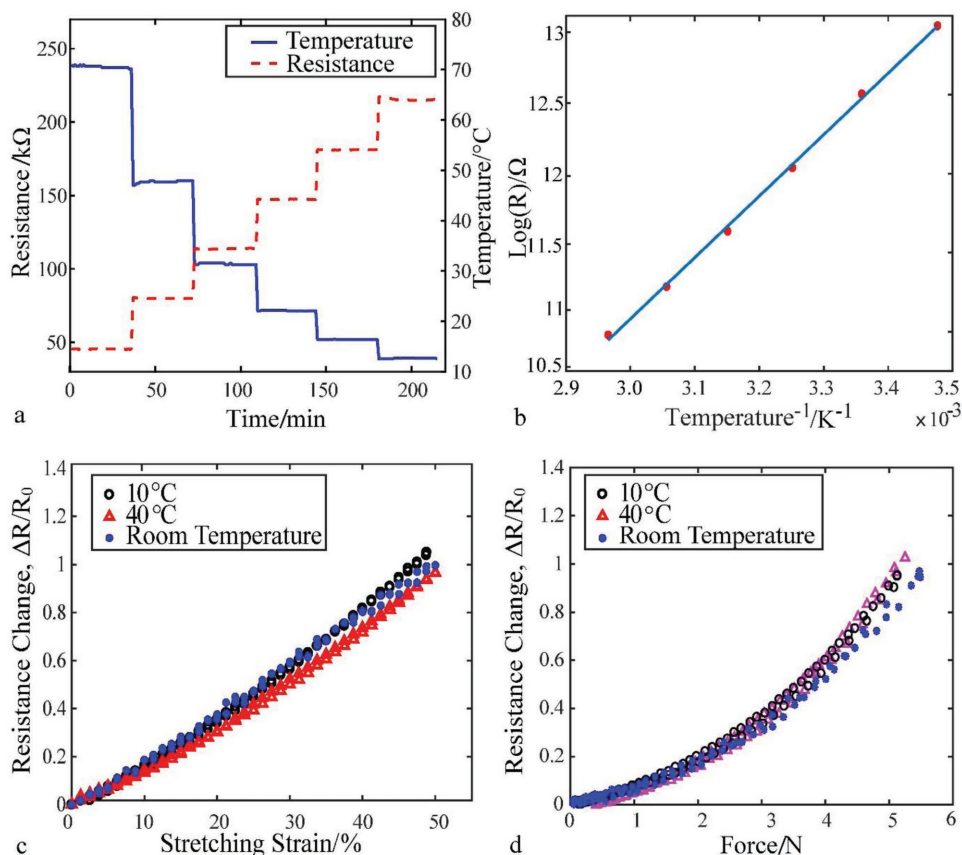


Figure 6. Characterization of the temperature influence on strain and force sensor resistance and sensitivity. a) Resistance change of strain and force sensors in a humidity chamber at 40% relative humidity with a temperature range from 15.0 to 65.0 °C. b) Log of resistance ($\log(R)$) as a function of the inverse of temperature (T^{-1}) and its linear fit. c) Strain sensor resistance change ($\Delta R/R_0$) as a function of strain at 10.0 °C, room temperature, and 40.0 °C. d) Force sensor resistance change ($\Delta R/R_0$) as a function of force at 10.0 °C, room temperature, and 40.0 °C.

and 40.0 °C. Figure 6c shows that when the strain sensor is stretched and released at all temperatures, the linearity and gauge factor variation is less than 10%. This property also holds true for force sensor, as is plotted in Figure 6d.

2.4.2. Humidity

Another potential influence on sensor resistance is humidity. Due to the penetration of water vapor into the electrolyte solution through the silicone substrate, the sensors are expected to have lower resistance in humid environments. The decrease in resistance is mainly due to two effects. First, the absorption of water from air increases the channel cross-sectional area. Second, the adding of water vapor to the KI-Gly solution decreases the liquid viscosity and thus increases its conductivity. Since the cross-sectional area change caused by channel inflation is relatively small, the conductivity change is the main reason for the sensor resistance change.

We tested the resistance of strain sensors within a temperature–humidity chamber at two different humidity levels at 25.0 °C, and compared it to the sensor at room conditions. As plotted in Figure 7a, the sensor resistance decreases exponentially under 60.0% or 80.0% relative humidity (RH), and the rate becomes

faster in a higher humidity environment. At 60.0% RH, the sensor needs more than 160 h to become stable, while at 80.0% RH it approaches equilibrium after 100 h. Moreover, sensors in a high humidity environment tends to have lower equilibrium resistance compared to those in a low humidity environment. To determine the joint influence of temperature and humidity on the sensor resistance within a short period of time, we measured the strain sensor resistance from 15.0 to 65.0 °C at various humidity levels, ranging from 40.0% RH to 80.0% RH (with a temperature increase of 10.0 °C h^{-1} , over a 6 h test period at each humidity level). Figure 7b shows that temperature is the dominating factor of the sensor resistance change. High humidity accelerates the resistance decrease at high temperature, but the short-term influence is not significant.

Similar to the influence of temperature, the humidity of the environment has an effect on the resistance, but does not change their sensitivity significantly. We characterized both force and strain sensors with the Instron after placing in the humidity chamber at 60.0% and 80.0% RH for 72 h, and at ambient humidity (40.0%-60.0% RH) (see Figure 7c,d). The strain sensors at 60.0% and 80.0% RH have a 10.0% lower sensitivity compared to the one in room environment, but not much difference between 60.0% or 80.0% relative humidity (RH), and the rate becomes

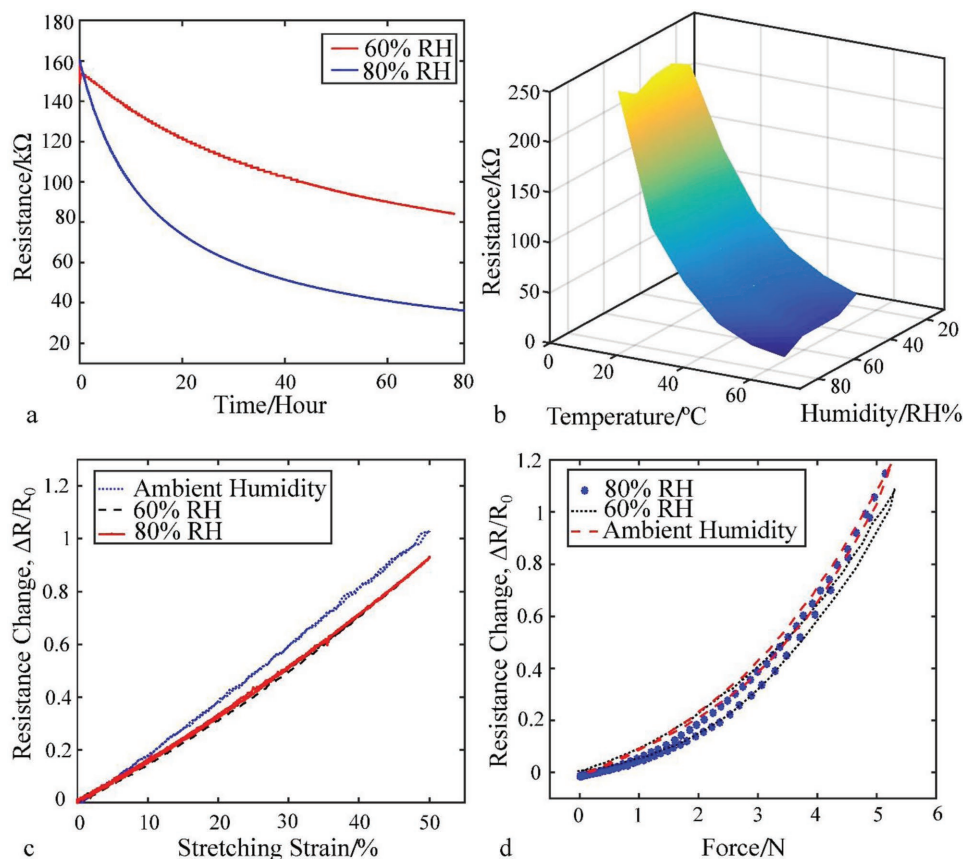


Figure 7. Humidity study of strain and force sensors. a) Resistance variation of strain sensor after placing in a temperature–humidity chamber for 72 h at 25.0 °C. b) 3D plot of temperature and humidity influence on sensor resistance, showing the combined impact of temperature and humidity on sensor resistance. c,d) Strain and force sensor resistance change ($\Delta R/R_0$) at ambient humidity conditions, and after placing in 60.0% RH and 80.0% RH environment for 72 h, showing the stability of sensitivity for both sensors at various humidity conditions.

2.5. Proof of Concept Demonstration

To demonstrate the functionality of the conductive liquid strain and force sensors as wearable devices, we applied both sensors to a human hand to observe real-time finger motions and force generation during hand activities.

First, the strain sensors were placed on the proximal interphalangeal joint (PIP) and the metacarpophalangeal joint (MCP) to detect the strains from a bending finger (Figure 8a). For ground truth, we used a motion capture system (Qualisys) to track the finger motion and a Visual 3D software to calculate the joint angles. Figure 8b demonstrates the measurements of the strain sensors on both joints when forming a closed fist from relaxed fingers repeatedly. The sensor signals are compared to the joint angle variations calculated from the motion capture data. The peak of each pulse represents the bending motion of the finger, and the lowest value represents the finger's relaxed state. During this movement, the MCP had a larger bending-induced extension than the PIP. The sensor placed at the MCP had a maximum resistance change of 45%, which was more than twice of that of the PIP sensor. Comparing the sensor signals to the motion capture data, the plot shows that the sensors were able to follow the instantaneous change of finger positions and detect the relative magnitude

of the finger bending angles. Furthermore, we captured the hand motion while performing an activity of piling five 25.0 g cubes. The sensor resistance changes of the PIP and the MCP are shown in Figure 8c. The MCP exhibited a slightly larger bending compared to the PIP, with a resistance increase of 13% and 10%, respectively. Relating the sensor signal to the motion capture video, we identified that each pulse represents the process of picking up a cube and piling it on others. For each grasping attempt, there existed two voltage peaks that indicated a joint angle adjustment during this time interval.

Second, force sensors were placed on finger tips to measure the force when grasping objects of different weights. Figure 8d shows the placement of a force sensor at the fingertip holding a beaker. To demonstrate the stability of the sensor measurements at different temperatures, we compared force measurements for the cases of grasping a 25.0 g ice cube and a 25.0 g room temperature weight. As plotted in Figure 8e, the resistance change for the case of grasping a room temperature weight and an ice cube were similar, and both showed a maximum resistance change of 15%. From the characterization plot of the force sensor in previous section, a resistance increase of 15% corresponds to a normal force of approximately 1.3 N. We also conducted an experiment of holding an empty water bottle and pouring in water gradually to study the reaction of the sensor

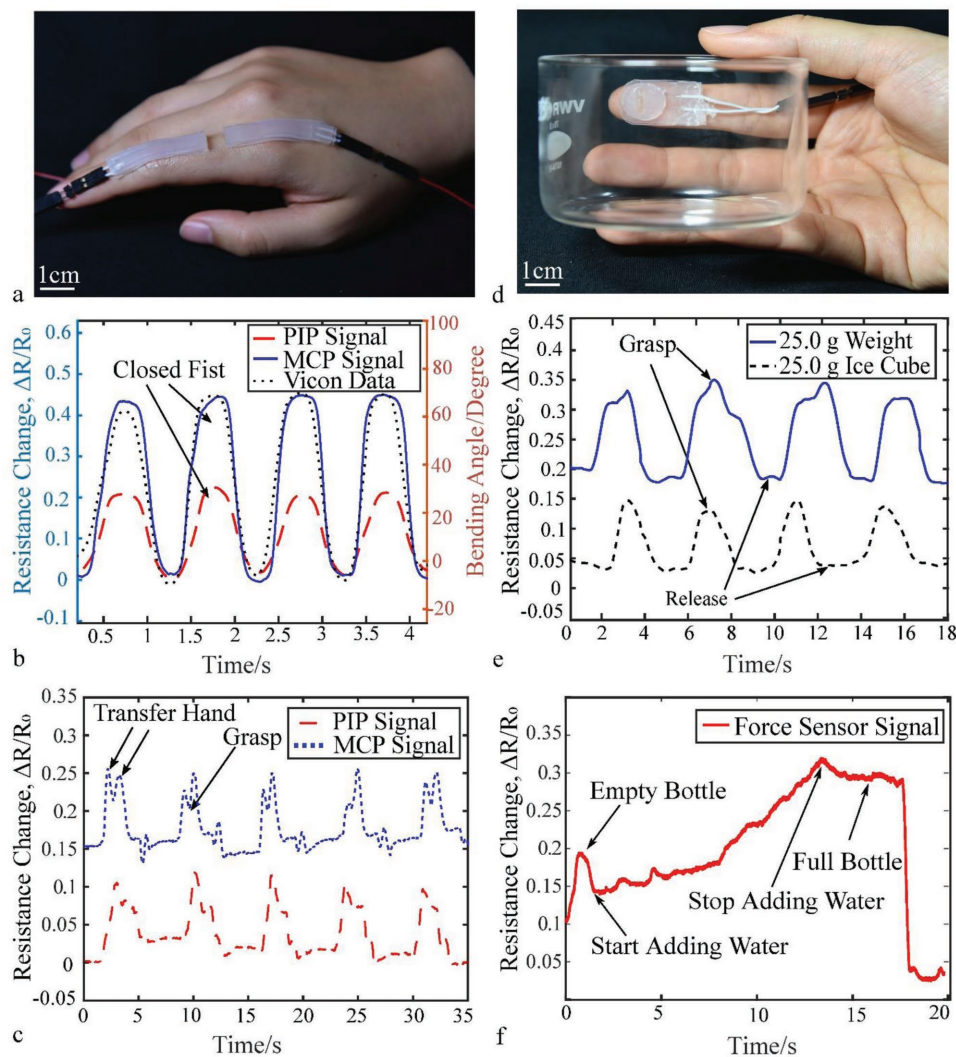


Figure 8. Demonstration of the functionalities of the strain and force sensors as wearable devices for human motion detection. a) Strain sensors placed at the PIP and the MCP of the index finger. b) Strain sensor detections of MCP and PIP movements with closed fist and extended fingers, with the Qualisys camera tracking results as a reference. c) Strain sensor detection of MCP and PIP movements during the activity of picking up and piling five 25.0 g 3D printed cubes. d) Force sensor attached to index fingertip. e) Force detection of repeatedly picking up 25.0 g room temperature weights and ice cubes, demonstrating the sensor functionality at different temperatures. f) Force measurement while pouring water into an empty water bottle at various speeds.

to a varying load. As shown in Figure 8f, we observed an initial resistance increase when the water bottle was picked up. The resistance increased gradually as water was poured into the bottle, indicating a larger force was applied.

3. Conclusion

In this paper, we first introduced a novel biocompatible conductive liquid (KI-Gly solution) for wearable sensing devices. The KI-Gly solution is highly stable in a silicone substrate, with a higher conductivity and lower viscosity compared to previously used electrolyte solutions. We embedded the conductive liquid into a silicone elastomer substrate and developed soft fluidic wearable strain and force sensors. Both sensors are highly flexible and durable for at least 1000 cycles. These sensors

have high sensitivities, are highly linear, and have bandwidth appropriate for human motion detections (5 Hz for the strain sensors, and 50 Hz for the force sensors).

Specifically, the force sensor was developed with a novel multilayer structure, which greatly improved the linearity and hysteresis that has long existed in fluidic soft sensors. By adding microcylinder fillers to the channel and increasing the stiffness of the substrate material, we improved the sensitivity at low forces and alleviated its nonlinear behavior at high forces. By tuning the substrate stiffness and the liquid flow volume, we decreased the hysteresis during load and release processes. Moreover, from the theoretical model predictions and experimental validations, we provided possible methods to tune the sensitivity based on various sensing ranges for different applications: by tuning the microfiller radius, substrate thickness, and substrate material stiffness.

We also found that the novel conductive liquid sensors baseline resistances fluctuate as temperature and humidity of the environment vary, but their sensitivities are reasonably stable. This property guarantees the functionality of the sensor at various environmental conditions. We demonstrated the capability of both strain and force sensors as wearable devices to detect human hand motions. The sensors accurately monitored the finger movements and interaction forces generated during hand activities and successfully proved their functionality at different temperatures. The high biocompatibility, stability, and accurate sensing performance would make our sensors not only promising for motion capture, but also for future development of health monitoring devices, surgical instruments, and human-machine interaction devices.

4. Experimental Section

Preparation of Conductive Liquid: The conductive liquid was prepared by mixing potassium iodide (KI) (5.5 g) (Sigma-Aldrich, NJ, USA) and glycerol (10 mL) (BDH1172, VWR Analytical, USA) with a planetary mixing machine (ARE-310, THINKY, USA) for 20 min.

Strain Sensor Fabrication Process: The strain sensor was fabricated with the molding, bonding, and injection techniques. The casting molds (channel patterned mold and flat mold) were prepared using a 3D printer (Objet Connex500, Stratasys, Edina, MN, USA). Silicone insulated wires (3169, Adafuit Industries LLC, NYC, USA) were first loaded into the 3D printed molds to improve the wire-sensor connection, as shown in Figure S4 in the Supporting Information. Then liquid silicone rubber Ecoflex 00-30 (Smooth-on, PA, USA) was poured into the flat mold and the channel-featured mold. Liquid silicone was cured in an oven for 20 min at 60.0 °C. Subsequently, the two separate parts of the sensor were wet bonded by spin-coating a 100 µm layer of liquid silicone on top of the flat base (2000 rpm, 30 s), and left to cure. Finally, the conductive liquid was injected into the microchannel with two syringes, one for liquid injection, and the other for air extraction. Figure S4 in the Supporting Information shows a strain sensor fabrication process.

Force Sensor Fabrication Process: The force sensor contains two functional layers: a sensing layer and a force amplification layer. The silicone insulated wires were loaded into the 3D printed mold first. Then two parts of the sensing layer were molded with the silicone mixture, a 3:1 ratio of 10:1 PDMS (Slygard 184, Dow Corning, MI, USA) and Ecoflex 0030. The force amplification base layer was molded with Ecoflex 0010 (Smooth-on, PA, USA). After curing, the microfillers were placed along the microchannel embedded in the sensing layer manually. These cylindrical fillers were prepared by cutting 0.5 mm diameter PMMA optical fiber in to 1 mm length cylinders with a diode pumped solid state laser (Oxford Laser, Industrial System, UK). The two sensing layer bases were then plasma bonded together, and the conductive liquid was injected into the microchannel with syringes. After finishing the sensing layer, Ecoflex 0030 was spin-coated onto the sensing layer to wet bond the previously molded force amplification layer. Finally, the UV curable adhesive (Henkel 36 480, Loctite 3943, CT, USA) was injected into the chamber between force amplification layer and the sensing layer with syringes, and was cured under UV light for 1 min. Figure S5 in the Supporting Information shows the force sensor fabrication process.

Supporting Information

Supporting Information is available from the Wiley Online Library or from the author.

Acknowledgements

This work was supported by NIH/NICHD 1R01HD090985-01, awarded to Harvard University and Boston Children's Hospital, and also by the Wyss Institute for Biologically Inspired Engineering at Harvard University.

Conflict of Interest

The authors declare no conflict of interest.

Keywords

biocompatible sensors, fluidic soft sensors, wearable sensors

Received: October 6, 2018
Revised: November 15, 2018
Published online:

- [1] H. Zhao, K. O'Brien, S. Li, R. F. Shepherd, *Sci. Rob.* **2016**, 1, eaai7529.
- [2] R. L. Truby, M. Wehner, A. K. Grosskopf, D. M. Vogt, S. G. M. Uzel, R. J. Wood, J. A. Lewis, *Adv. Mater.* **2018**, 30, 1706383.
- [3] P. Polygerinos, N. Correll, S. A. Morin, B. Mosadegh, C. D. Onal, K. Petersen, M. Cianchetti, M. T. Tolley, R. F. Shepherd, *Adv. Eng. Mater.* **2017**, 19, 1700016.
- [4] E. L. White, J. C. Case, R. K. Kramer, *Sens. Actuators, A* **2017**, 253, 188.
- [5] C. Majidi, *Mech. Eng.* **2016**, 138, S17.
- [6] R. Rahimi, M. Ochoa, W. Yu, B. Ziaie, *ACS Appl. Mater. Interfaces* **2015**, 7, 4463.
- [7] O. Atalay, A. Atalay, J. Gafford, C. Walsh, *Adv. Mater. Technol.* **2018**, 3, 1700237.
- [8] G. Shi, Z. Zhao, J.-H. Pai, I. Lee, L. Zhang, C. Stevenson, K. Ishara, R. Zhang, H. Zhu, J. Ma, *Adv. Funct. Mater.* **2016**, 26, 7614.
- [9] J. Ulmen, M. Cutkosky, presented at *2010 IEEE Int. Conf. on Robotics and Automation*, Anchorage, USA, May **2010**.
- [10] H.-H. Chou, A. Nguyen, A. Chortos, J. W. F. To, C. Lu, J. Mei, T. Kurosawa, W.-G. Bae, J. B.-H. Tok, Z. Bao, *Nat. Commun.* **2015**, 6, 8011.
- [11] V. Arabagi, O. Felfoul, A. H. Gosline, R. J. Wood, P. E. Dupont, *IEEE Sens. J.* **2016**, 16, 1294.
- [12] H. Fang, K. J. Yu, C. Gloschat, Z. Yang, E. Song, C.-H. Chiang, J. Zhao, S. M. Won, S. Xu, M. Trumpis, Y. Zhong, S. W. Han, Y. Xue, D. Xu, S. W. Choi, G. Cauwenberghs, M. Kay, Y. Huang, J. Viveri, I. R. Efimov, J. A. Rogers, *Nat. Biomed. Eng.* **2017**, 1, 0038.
- [13] M. D. Dickey, *Adv. Mater.* **2017**, 29, 1606425.
- [14] J. W. Boley, E. L. White, G. T.-C. Chiu, R. K. Kramer, *Adv. Funct. Mater.* **2014**, 24, 3501.
- [15] M. D. Dickey, R. C. Chiechi, R. J. Larsen, E. A. Weiss, D. A. Weitz, G. M. Whitesides, *Adv. Funct. Mater.* **2008**, 18, 1097.
- [16] J. C. Yeo, J. Yu, Z. M. Koh, Z. Wang, C. T. Lim, *Lab Chip* **2016**, 16, 3244.
- [17] R. K. Kramer, C. Majidi, R. J. Wood, presented at *2011 IEEE Int. Conf. on Robotics and Automation*, Shanghai, China, May **2011**.
- [18] Y. Park, B. Chen, R. J. Wood, *IEEE Sens. J.* **2012**, 12, 2711.
- [19] H. O. Michaud, L. Dejace, S. de Mulatier, S. P. Lacour, presented at *2016 IEEE/RSJ Int. Conf. on Intelligent Robots and Systems*, Daejeon, Korea, October **2016**.
- [20] A. Anderson, Y. Menguc, R. J. Wood, D. Newman, *IEEE Sens. J.* **2015**, 15, 6229.

- [21] Y. Mengüç, Y.-L. Park, H. Pei, D. Vogt, P. M. Aubin, E. Winchell, L. Fluke, L. Stirling, R. J. Wood, C. J. Walsh, *Int. J. Rob. Res.* **2014**, *33*, 1748.
- [22] J. Chossat, V. Y. Tao, Y.-L. Duchaine, Y.-L. Park, presented at *2015 IEEE Int. Conf. on Robotics and Automation*, Seattle, USA, May **2015**.
- [23] S.-H. Zhang, F.-X. Wang, J.-J. Li, H.-D. Peng, J.-H. Yan, G.-B. Pan, *Sensors* **2017**, *17*, 2621.
- [24] D. Y. Choi, M. H. Kim, Y. S. Oh, S.-H. Jung, J. H. Jung, H. J. Sung, H. W. Lee, H. M. Lee, *ACS Appl. Mater. Interfaces* **2017**, *9*, 1770.
- [25] F. L. Hammond, Y. Menguc, R. J. Wood, presented at *2014 IEEE/RSJ Int. Conf. on Intelligent Robots and Systems*, Chicago, USA, September **2014**.
- [26] Y.-L. Park, D. Tepayotl-Ramirez, R. J. Wood, C. Majidi, *Appl. Phys. Lett.* **2012**, *101*, 191904.
- [27] Y.-L. Park, C. Majidi, R. Kramer, P. Bérard, R. J. Wood, *J. Micromech. Microeng.* **2010**, *20*, 125029.
- [28] A. Hammadi, *Int. J. Thermophys.* **2004**, *25*, 89.
- [29] D. E. Goldsack, R. Franchetto, *Can. J. Chem.* **1977**, *55*, 1062.
- [30] H. D. B. Jenkins, Y. Marcus, *Chem. Rev.* **1995**, *95*, 2695.
- [31] Smooth-On, Ecoflex Series, https://www.smoothon.com/tb/files/ECOFLEX_SERIES_TB.pdf (accessed: September 2018).
- [32] H.-J. Freund, *Prog. Brain Res.* **1986**, *64*, 287.
- [33] D. Tepáyotl-Ramírez, T. Lu, Y.-L. Park, C. Majidi, *Appl. Phys. Lett.* **2013**, *102*, 044102.
- [34] H.-S. Shin, J. Ryu, C. Majidi, Y.-L. Park, *J. Micromech. Microeng.* **2016**, *26*, 025011.